Optimized design of three-dimensional multi-shell $Fe_3O_4/SiO_2/ZnO/ZnSe$ microspheres with type II heterostructure for photocatalytic applications

Dandan Wang[a,b,c,1], Donglai Han[d,1], Zhu Shi[c], Jian Wang[c], Jinghai Yang[c,*], Xiuyan Li[c,*], Hang Song[a]

[a] Changchun Institute of Optics, Fine Mechanics and Physics, Chinese Academy of Sciences, Changchun 130033, PR China
[b] University of Chinese Academy of Sciences, Beijing 100049, PR China
[c] Key Laboratory of Functional Materials Physics and Chemistry of the Ministry of Education, Jilin Normal University, Changchun 130103, PR China
[d] School of Materials Science and Engineering, Changchun University of Science and Technology, Changchun, 130022, PR China

ABSTRACT

Here, a new three-dimensional (3D) multi-shell $Fe_3O_4/SiO_2/ZnO/ZnSe$ (FSZ-ZnSe) photocatalyst with a type II heterostructure was successfully produced by a convenient synthetic route. The amount of ZnSe particles can be regulated by varying the reactant concentration, and five kinds of FSZ-ZnSe samples (FSZ-ZnSe0, FSZ-ZnSe1, FSZ-ZnSe2, FSZ-ZnSe3 and FSZ-ZnSe4) were obtained. The photocatalytic performances of all as-prepared samples under UV and visible light irradiation were evaluated by the photocatalytic elimination of rhodamine B (RhB) aqueous solution. No matter which light source was used, the FSZ-ZnSe3 sample exhibited enhanced photocatalytic activity in comparison with other samples, benefiting from the sensitization of a proper amount of ZnSe particles, which not only facilitated the separation of photo-induced carriers but also extended the light absorption. Moreover, compared to visible light radiation, the FSZ-ZnSe3 sample under UV light showed remarkably enhanced degradation efficiency toward RhB base on the Z-scheme type transfer of photo-generated electron-hole pairs. The Z-scheme mechanism was confirmed using radical trapping experiments and hydroxyl radical (·OH) formation determination study. Meanwhile, the FSZ-ZnSe3 sample exhibited excellent magnetic response and high stability during the recycling photocatalytic experiments.

1. Introduction

With the growing awareness of environmental protection and the shortage of clean water sources, photocatalytic degradation of organic pollutants in water has become a hot research topic due to its high efficiency compared to traditional treatment methods, e.g. adsorption, coagulation, and membrane separation [1,2]. In view of the omnipresent existence of semiconductor minerals, such as TiO_2, ZnO, SnO_2, WO_3, CdS, SnS, and ZnS, the treatment of wastewater by using semiconductor catalysts has been widely investigated [3–7]. Among various semiconductor materials, ZnO has many useful characteristics, such as easy access, good biocompatibility, large piezoelectric constant and perfect electron mobility (205–300 cm^2 V/s), which is higher than that of TiO_2 (0.1–4 cm^2 V/s) [8]. Most importantly, hierarchically self-assembled 3D ZnO superstructures have been extensively investigated because of their outstanding optical and catalytic properties [9,10]. Moreover, 3D ZnO architectures can prevent structural aggregation, which preserves the large catalytically active surface area and the

interstitial channels [8]. This kind of interstitial channels permit the diffusion of chemicals into the structure, thereby improving the efficiency of surface reactions. However, the photocatalytic activity of ZnO under UV light is unsatisfactory as a result of the high recombination rate of photo-generated carriers, and ZnO under visible light is almost no activity duo to the high band gap (3.37 eV) [4,11].

Recently, co-catalysis and heterostructures with other semiconductor materials have been extensively studied to simultaneously improve the optical absorption capacity and the tendency towards charge recombination of ZnO material. ZnO/CdX (X = S, Se, or Te) heterostructures have been reported for this purpose [12–14]. Nevertheless, these cadmium compounds are carcinogenic. As one of the important II–VI semiconductors, ZnSe is an environmentally friendly and low-cost, which has for a long time been expected to be a promising material for photocatalysis application owing to its appropriate optical band gap (Eg = 2.80 eV) and giant photosensitivity [15,16]. Furthermore, the valence and conduction bands of ZnSe are staggeredly aligned relatively to those of ZnO, which make ZnSe material an ideal

candidate to produce type II heterostructures with ZnO. For example, Chen et al. have reported that ZnO/ZnSe heterostructures can remarkably promote the separation of photo-generated carriers and extend the absorption range of ZnO towards visible light [17,18].

On the other hand, manipulation and separation of ZnO-based materials from the treated systems restricts their large-scale applications. Although filtration, centrifuge, and fixation of photocatalysts provide solutions for this drawback, these means usually increase use-cost or reduce the activity of photocatalysts due to the dramatic reduction of the active surface area caused by fixation [19]. One effective approach is to separate and recycle the ZnO-based materials by synthesizing novel composite materials with magnetic performance [20]. By using an appropriate magnetic field, the magnetic separation can provide a convenient way for recycling of these materials within a short time.

Herein, to take a further step in the application of ZnO-based materials for a highly efficient, recoverable, stable, and cost-effective photocatalyst, we reported for the first time the optimized design of 3D multi-shell FSZ-ZnSe microspheres with ZnO/ZnSe type II heterostructure for photocatalytic applications. Based on our previous study, Fe_3O_4 core and SiO_2 layer in this new photocatalyst were used as magnetic carrier and electronic barrier, respectively [21,22]. And ZnO nanorod-layer with well-dispersed ZnSe particles served as photocatalytic layer. The amount of ZnSe particles was controllably synthesized by a facile solution-phase surface modification. The photocatalytic performances of samples under UV and visible light irradiation were evaluated by the photocatalytic elimination of rhodamine B (RhB). Accordingly, the electron transfer models combined with band structure alignment were used to explain their differences in photocatalytic activities. Moreover, using an external magnetic field, the photocatalyst can be easily recycled without significant decrease in the photocatalytic activity.

2. Experimental section

2.1. Sample preparation

All chemicals were of analytical grade and were used as received without further purification.

Magnetic 3D multi-shell $Fe_3O_4/SiO_2/ZnO$ microspheres were firstly prepared by simple methods as our previous work described [14]. The as-obtained Fe_3O_4, Fe_3O_4/SiO_2, $Fe_3O_4/SiO_2/ZnO$-seeds and $Fe_3O_4/SiO_2/ZnO$ samples were denoted as F, FS, FSz and FSZ-ZnSe0 in the following. Subsequently, a solution-phase surface modification was performed to deposit different amount of ZnSe particles on FSZ-ZnSe0 sample as follows: a Se^{2-} source solution was first prepared by mixing a certain amount of Se powder and $NaBH_4$ in 60 mL of deionized water. The solution was stirred until it turned clear. Then, 0.1 g of FSZ-ZnSe0 powder was added into the Se^{2-} source solution, after mechanically stirred for 15 min, the mixture was heated at 60 °C for 3 h. The products were washed with distilled water and absolute ethanol, respectively, and then dried at 60 °C.

The obtained products at different growth conditions from low to high concentration of Se^{2-} source solution were labeled as FSZ-ZnSe1 (Se: 0.005 g, $NaBH_4$: 0.05 g), FSZ-ZnSe2 (Se: 0.01 g, $NaBH_4$: 0.1 g), FSZ-ZnSe3 (Se: 0.015 g, $NaBH_4$: 0.15 g) and FSZ-ZnSe4 (Se: 0.02 g, $NaBH_4$: 0.2 g), respectively.

2.2. Characterization

Field emission scanning electron microscopy (FESEM, JEOL 7800F) and transmission electron microscopy (TEM, FEI Tenai G^2 F20) were used to characterize the morphology and structure of the obtained products. Energy dispersive X-ray spectroscopy (EDX) was also performed by the FEI Tenai G^2 F20 microscope linked with an Oxford Instruments X-ray analysis system. The crystal structure of the as-prepared materials was analyzed by a D/max-2500 copper rotating-anode X-ray powder diffraction with Cu-Kα radiation of wavelength λ = 1.5406 Å (40 kV, 200 mA). The textural properties of samples were determined by the Brunauer Emmett Teller (BET) method using N_2 adsorption-desorption isotherms by a Nova l000 analyzer. UV–vis diffuse reflection spectra (DRS) of the dry-pressed disk samples were obtained with a Perkin-Elmer Lambda 900 spectrometer. Photoluminescence (PL) was measured at room temperature by using a Renishaw inVia micro-PL spectrometer (He-Cd laser) with an excitation wavelength of 325 nm. The magnetization curves of the samples were characterized by using a vibrating sample magnetometer (VSM, Lake Shore 7407) at room temperature.

2.3. Photocurrent measurements

Photocurrent was determined by a computer-controlled electro-chemical work station (CHI-660C Instruments, China) in a standard three-compartment cell containing 25 mL of 0.5 M Na_2SO_4 solution. The as-prepared samples coated on the indium-tin oxide glass (1.0 cm × 4.0 cm) were used as the working electrode, a Pt minigrid as the counter electrode, and a saturated calomel electrode (SCE) as the reference electrode. At applied potential of −0.5 V versus SCE, photocurrents of the samples were obtained under UV light using a high-pressure mercury lamp (250 W, main emission wavelength at 365 nm), and visible light using a Xe lamp (CEL-HXUV300 300 W) by with a 420 nm cutoff filter.

2.4. Photocatalytic test

The photocatalytic activities of the as-prepared samples under UV and visible light irradiation were evaluated towards degradation of RhB. The light sources were the same as that used in photocurrent measurement. The weight of catalyst used for each experiment was 0.03 g, which was placed in the reactor and then 100 mL of aqueous RhB solution (7 mg/L) was injected. The obtained suspension was mechanically stirred for 20 min in the dark to reach an adsorption-desorption equilibrium between the catalyst and RhB molecules. Subsequently, the light source was switched on, and the reaction mixture was continuously mechanically stirred and then 2 mL of aliquots was withdrawn from the irradiated suspension every 20 min. The photocatalyst was separated by using a magnet before absorbance measurement, where the absorbance at 555 nm was measured using an UV–vis spectrophotometer (UV-5800PC, Shanghai Metash Instruments Co., Ltd). The concentration of RhB in the degraded sample was determined using a calibration curve (concentration vs. absorbance) prepared using known concentrations of RhB and the percentage degradation was then calculated. After washing with ethanol and deionized water for three times, the recycled catalyst was dispersed again in RhB solution, and the new photocatalytic cycle began.

2.5. Determination of hydroxyl radical (·OH) formation

The ·OH formed in the photocatalytic reaction was detected by the fluorescence technique with terephthalic acid (TA) as a probe molecule. TA reacted with ·OH to produce a highly fluorescent product, 2-hydroxyterephthalic acid (TA-OH), and the fluorescence intensity of TA-OH peak was proportional to the amount of ·OH radicals. The experimental procedure as follows: at ambient temperature, 0.03 g of the sample was dispersed in a mixed aqueous solution of 5×10^{-4} M TA and 2×10^{-3} M NaOH. Subsequently, the reaction mixture was subjected to light irradiation. Sampling was performed every 20 min for analysis and the photocatalyst was separated by using a magnet. The solution was analyzed on a Hitachi F-4600 fluorescence spectrophotometer, and the fluorescence signal at 425 nm arising from TA-OH at the excitation wavelength of 315 nm was obtained.
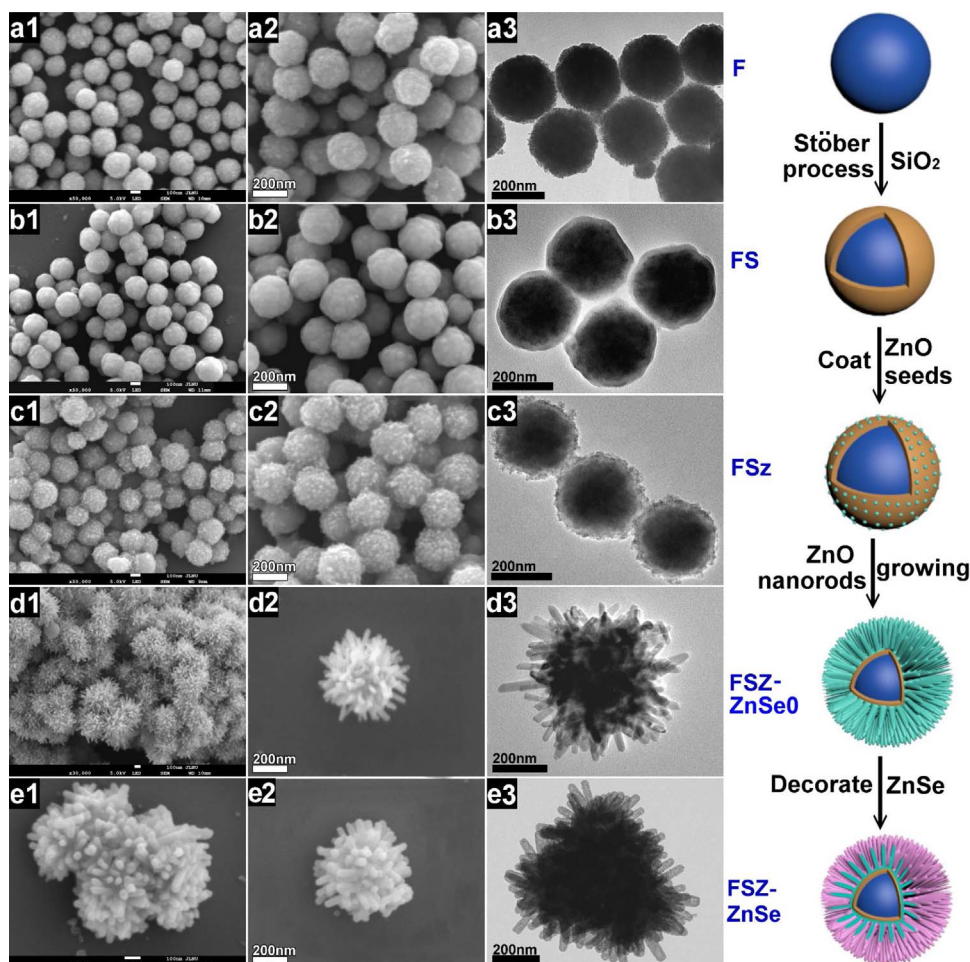
Fig. 1. Left: Low-magnification SEM, high-magnification SEM and TEM images of (a1-3) F, (b1-3) FS, (c1-3) FSz, (d1-3) FSZ-ZnSe0, (e1-3) FSZ-ZnSe3. Right: Schematic image of the formation of multi-shell FSZ-ZnSe microsphere.

3. Results and discussion

3.1. Morphologies and phase structures

Low-magnification SEM, high-magnification SEM and TEM images of F, FS, FSz, FSZ-ZnSe0 and FSZ-ZnSe3 samples are given in Fig. 1a–e, respectively. And the schematic image of the formation of multi-shell FSZ-ZnSe microsphere is shown in right column of Fig. 1. As presented in Fig. 1a1–3, the obtained F microspheres are uniform with a mean diameter of about 240 nm. The SEM images of FS product (Fig. 1b1 and b2) show that the formed SiO_2 uniformly coated on F core. It can be clearly seen from Fig. 1b3 that the average thickness of SiO_2 layer is about 20 nm and the size of FS microsphere is about 280 nm. As shown in Fig. 1c1 and c2, FSz microsphere has a rougher surface, suggesting the deposited ZnO seeds on FS microsphere are relatively looser in conglomeration. TEM image in Fig. 1c3 indicates the ZnO seed layer is uniform and its thickness is about 8 nm. Fig. 1d1 and d2 show the high-density ZnO nanorods vertically align on FSz microspheres and the urchin-like FSZ-ZnSe0 microspheres are formed. Combined with the TEM image in Fig. 1d3, it can be confirmed that the ZnO nanorod has a smooth surface, its diameter and length are about 40 nm and 150 nm, respectively.

Fig. 1e1 and e2 display the SEM images of FSZ-ZnSe3 product, revealing that the formed ZnO/ZnSe nanorod keeps the similar morphology of ZnO nanorod templates. Fig. 1e3 exhibits that the surface of ZnO/ZnSe nanorod is rougher, and its diameter is about 50 nm. The SEM images of FSZ-ZnSe1, FSZ-ZnSe2 and FSZ-ZnSe4 samples are given in Fig. S1a, b, and d, respectively. Obviously, the deposited content of ZnSe particles and the diameter of ZnO/ZnSe nanorod increase with the

increase in the concentrations of Se^{2-} solution.

Fig. 2a shows TEM image of a single FSZ-ZnSe3 microsphere, and the images with different color in the right column show the Fe-, Si-, O-, Zn, and Se-enriched areas in TEM image (a), respectively. It can be seen from these images that FSZ-ZnSe3 microsphere with a expected multi-shell structure was successfully prepared. A more detailed investigation is presented in Fig. 2b, the size of ZnSe particles is 5 nm on average, and two types of lattice fringes is observed. One set of the planar spacing is about 0.26 nm corresponding to the (002) plane of hexagonal wurtzite ZnO (JCPDS card No. 36-1451), and another set of the fringes' spacing is measured to be about 0.32 nm which corresponds to the (111) lattice spacing of cubic ZnSe (JCPDS card No. 37-1463). Above information verifies that ZnSe particles indeed grow over ZnO nanorod, forming ZnO/ZnSe heterostructure. In addition, the spatial distribution of the compositional elements within ZnO/ZnSe nanorod was obtained by EDX line scans along the nanorod's radial direction. Three signal peaks in Zn, O, and Se are shown in Fig. 2c. A higher intensity of Se primary appears in the shell region, while O signal is mainly confined within the core area. The Zn signal almost emerges along the nanorod's radial direction, especially within the core domain. This is consistent with the ZnO-core-ZnSe-shell nanorod layout observed in the HRTEM image.

Fig. 3aI shows the XRD pattern of F sample, all characteristic peaks are indexed to face-centered cubic structure Fe_3O_4 (JCPDS card No. 19-0629). As presented in Fig. 3aII, the diffraction peaks of FS sample are similar to the characteristic peaks of the parent F sample, except a broad and weak peak centered at 22° of 2θ corresponding to amorphous SiO_2 phase. There are some new characteristic peaks in XRD pattern of FSZ-ZnSe0 sample, as shown in Fig. 3aIII, which are indexed to the hexagonal wurtzite structure ZnO phase (JCPDS No. 36-1451). As
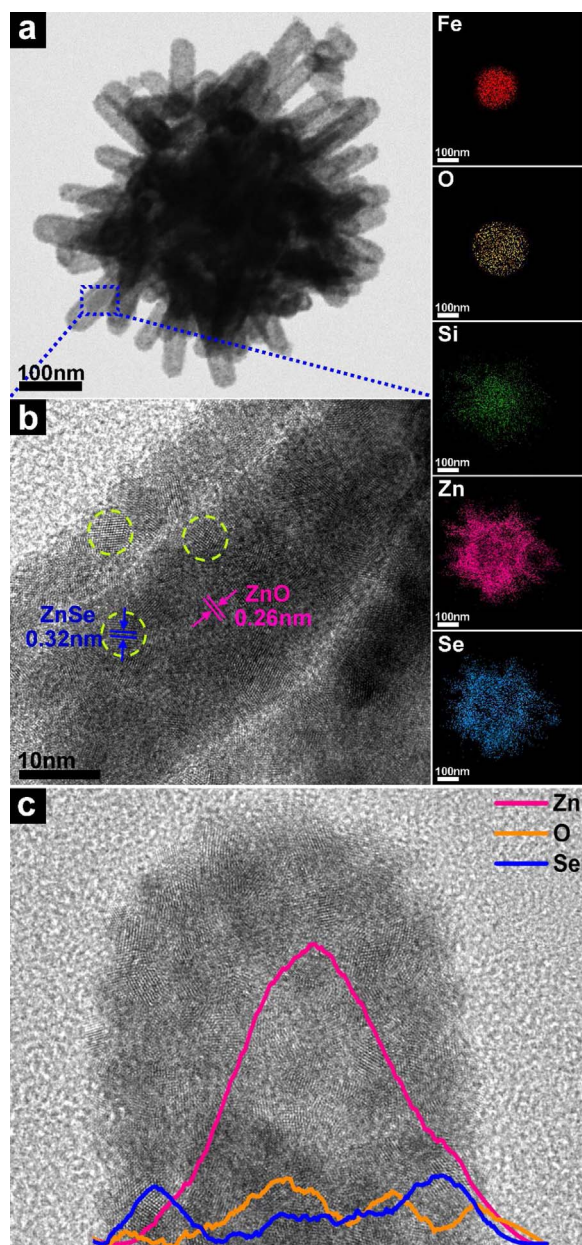
Fig. 2. (a) TEM image of a single FSZ-ZnSe3 microsphere; the right column presents the element mappings of Fe, Si, O, Zn, and Se in the region shown in TEM image (a), respectively, (b) HRTEM image and (c) representative EDX line scanning spectroscopy of ZnO/ZnSe nanorod in TEM image (a).
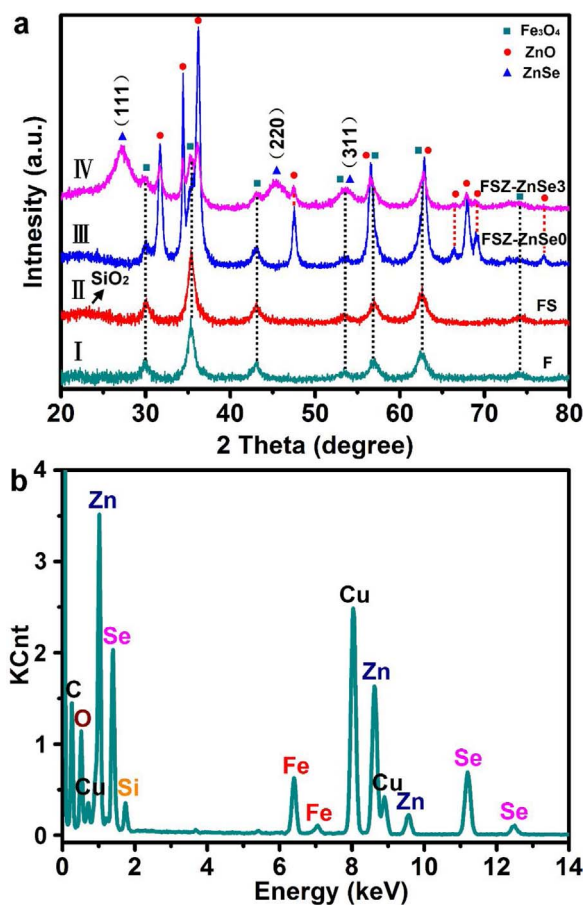

Fig. 3. (a) XRD patterns of F, FS, FSZ-ZnSe0 and FSZ-ZnSe3 samples and (b) EDX spectra of FSZ-ZnSe3 sample.
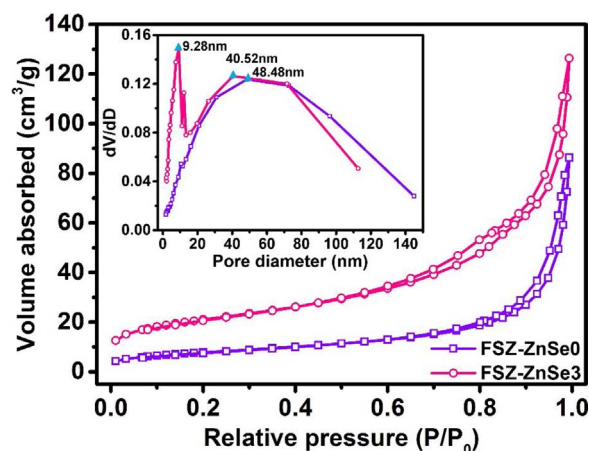

Fig. 4. N$_2$ adsorption-desorption isotherms and pore size distribution curves (inset) of FSZ-ZnSe0 and FSZ-ZnSe3 samples.

observed in Fig. 3aIV, the obvious diffraction peaks at 2θ = 27.23, 45.20 and 53.57° are assigned to (111), (220), and (311) crystal planes of the cubic zinc blend ZnSe structure (JCPDS No. 37-1463), respectively, indicating ZnSe crystal particles have been deposited on the FSZ-ZnSe0 microspheres. The EDX spectrum for FSZ-ZnSe3 sample is given in Fig. 3b. The peaks of Fe, Si, O, Zn, and Se elements are detected (the Cu and C signals come from the copper grid), and no other impurities can be observed, which is consistent with XRD.

3.2. BET surface area and pore size distributions

N$_2$ adsorption-desorption measurements were carried out to confirm the textural properties of the FSZ-ZnSe0, FSZ-ZnSe1, FSZ-ZnSe2, FSZ-ZnSe3 and FSZ-ZnSe4 samples. Fig. 4 shows the N$_2$ adsorption-desorption isotherms of FSZ-ZnSe0 and FSZ-ZnSe3 samples (The N$_2$ adsorption-desorption isotherms for FSZ-ZnSe1, FSZ-ZnSe2 and FSZ-

ZnSe4 samples are given in Fig. S2). According to IUPAC classification, these N$_2$ adsorption-desorption isotherms with H3 type hysteresis loop can be attributed to type IV isotherm, implying the mesopores properties [23]. Using the BJH method and the desorption branch of the N$_2$ isotherms, the calculated pore-size distribution curves of FSZ-ZnSe0 and FSZ-ZnSe3 samples are presented in the insert of Fig. 4. Both pore size distribution curves contain mesopores (2.0–50.0 nm) and macropores (> 50 nm). For FSZ-ZnSe0 sample, the main size of mesopores locates at 48.48 nm, which reflects basically slit-like pores within dense and uniform ZnO nanorod-layer. The mesopores of FSZ-ZnSe3 sample

Table 1
The textural properties of FSZ-ZnSe0, FSZ-ZnSe1, FSZ-ZnSe2, FSZ-ZnSe3 and FSZ-ZnSe4 samples.

Samples	SBET (m^2/g)	Vp (cm^3/g)	D (nm)
FSZ-ZnSe0	28.04	0.133	19.03
FSZ-ZnSe1	58.42	0.163	11.12
FSZ-ZnSe2	72.82	0.195	11.07
FSZ-ZnSe3	84.99	0.235	10.74
FSZ-ZnSe4	64.47	0.179	11.13

include two main sizes. The smaller mesopore at 9.28 nm may come from the fine aggregated pores formed between ZnSe particles and ZnO nanorods, while the larger mesopore at 40.52 nm results from ZnO/ZnSe nanorod-layer. The macropores for FSZ-ZnSe0 and FSZ-ZnSe3 samples are related to the pores formed between stacked microspheres.

Table 1 lists the textural properties of the tested samples, including BET-surface area (SBET), total pore volume (Vp) and mean pore diameter (D). Obviously, the estimated surface area and total pore volume in the order: FSZ-ZnSe0 < FSZ-ZnSe1 < FSZ-ZnSe4 < FSZ-ZnSe2 < FSZ-ZnSe3. But, the estimated mean pore diameters follow the opposite sequence: FSZ-ZnSe0 > FSZ-ZnSe1 > FSZ-ZnSe4 > FSZ-ZnSe2 > FSZ-ZnSe3. The above data illustrates that varying the amount of ZnSe particles significantly affects the specific surface area and mesoporous structure of products. Generally, the photocatalytic performance of the materials is highly dependent on the amount of surface that they have [24]. Therefore, the large surface area and a good mesoporous structure may make the FSZ-ZnSe3 sample a effective photocatalyst.

3.3. Optical properties

Fig. 5a shows the UV–vis diffuse reflectance spectra of FSZ-ZnSe0 and FSZ-ZnSe3 samples. In comparison with FSZ-ZnSe0 sample, FSZ-ZnSe3 sample exhibits enhanced absorption to visible light region. In order to clearly observe the differences between FSZ-ZnSe0 and FSZ-
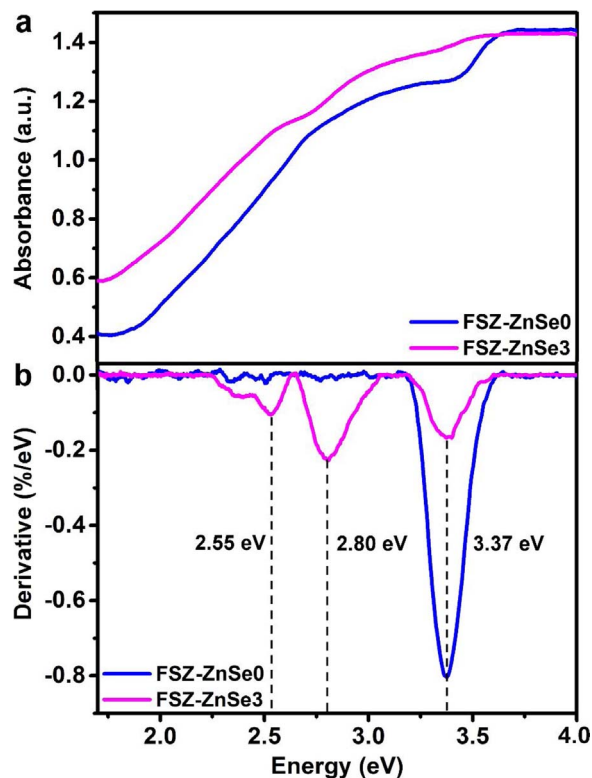

Fig. 5. (a) UV–vis diffuse reflectance spectra and (b) the corresponding derivative curves of FSZ-ZnSe0 and FSZ-ZnSe3 samples.
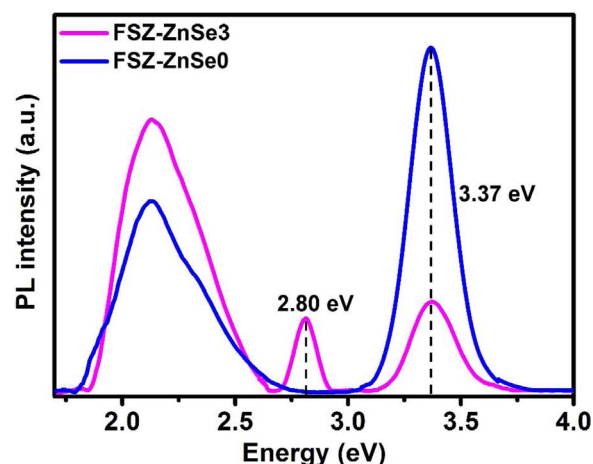

Fig. 6. Room-temperature PL spectra of FSZ-ZnSe0 and FSZ-ZnSe3 samples.

ZnSe3 samples, the spectra deriving from UV–vis diffuse reflectance spectra are shown in Fig. 5b. For FSZ-ZnSe0 sample, only one distinct peak at 3.37 eV is observed, which is a characteristic of wurtzite ZnO. Interestingly, there are three absorption peaks in the derivative spectrum of FSZ-ZnSe3 sample. The peaks at 3.37 and 2.80 eV are ascribed to ZnO and ZnSe, respectively. The new absorption peak at 2.55 eV may arise from the interfacial type II transition, involving the blend structure between the valence band of ZnSe and the conduction band of ZnO [18]. The transition at the type II interface between ZnO and ZnSe is adequate to the microstructural characterization for FSZ-ZnSe3 sample, and is responsible for the absorbed energy extension to the near infrared [25,26].

Fig. 6 exhibits the PL spectra of FSZ-ZnSe0 and FSZ-ZnSe samples. As is well known, the ultraviolet peaks at 3.37 eV in both PL spectra are ascribed to the near band edge (NBE) emission of ZnO, while the peaks at about 2.23 eV are associated with the defect emission of ZnO [27]. In the case of FSZ-ZnSe3 sample, a peak at 2.80 eV is designated to the NBE emission of ZnSe [28]. Note that the NBE emission peak of ZnO for FSZ-ZnSe3 sample is remarkably reduced. The main contribution is the staggered energy band alignment in ZnO/ZnSe type II hetero-nanostructure, which effectively suppresses the radiative recombination of photo-generated electrons and holes, and hence weakens the luminescence intensity [18,27]. Additionally, the defect emission of ZnO (at about 2.23 eV) in the PL spectra of FSZ-ZnSe3 sample slightly increases, which may be attributed to the Se induced defect emission in ZnO and the interfacial transition between ZnO and ZnSe due to the stock shift [18].

3.4. Photocurrent analysis

Fig. 7a and b show the photocurrent response of different FSZ-ZnSe samples under UV and visible light illumination, respectively. With the light irradiation on, the photocurrent sharply increases and then recovers to the initial state completely when the light is off, which can be ascribed to the fast diffusion of photo-excited electrons when the photo-excited holes are captured by hole-accepter in the electrolyte simultaneously [28,29]. Apparently, no matter which light source is used, FSZ-ZnSe1-4 samples show enhanced photocurrent signals in comparison with FSZ-ZnSe0 sample, which proves that ZnO/ZnSe type II heterostructure can promote the separation and migration of photo-generated carriers. Moreover, the photocurrent intensity increases gradually as the content of ZnSe is increased, after which it begins to decline with further increase in the content of ZnSe. Here, too much ZnSe particles not only induce recombination centers hindering the separation of the photo-generated carriers, but also block the ZnO nanorods array pores inhibiting generation and migration of the photo-induced carriers [30]. In conclusion, the obviously enhanced photocurrent response either
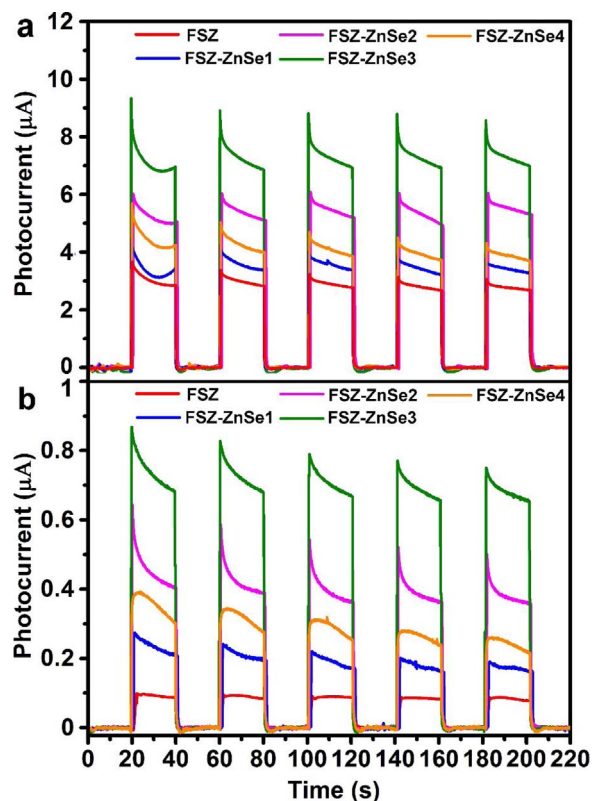
Fig. 7. Chopping UV (a) and visible light (b) photocurrent curves for different FSZ-ZnSe samples.

under UV or visible light implies that FSZ-ZnSe3 sample would exhibit good photocatalytic activity [31].

3.5. Photocatalytic activity

Fig. 8a shows the photodegradation efficiency activity of various types of FSZ-ZnSe samples under UV (solid line) and visible light (dotted line) irradiation. Quite evidently, the photolysis of RhB can be ignored, which is confirmed by the blank reaction (without photocatalysts). The photocatalytic degradation curves of RhB over time with FSZ-ZnSe3 sample as photocatalyst are given in Fig. 8b. No matter which light source was used, the typical absorption peak at 555 nm weakens gradually after 60 min, indicating the gradual removing of RhB by the FSZ-ZnSe3 photocatalysts. Fig. 8c shows the final photodegradation rate of RhB in presence of various samples. Regardless of UV or visible light irradiation, it can be noted that the photodegradation rates of RhB increase firstly with increasing the amount of ZnSe in FSZ-ZnSe samples, and the highest RhB decomposition ratio occurs for FSZ-ZnSe3 sample. For FSZ-ZnSe4 sample, further increasing the content of ZnSe leads to a decrease in the degradation rate of RhB. Hence, the photoactivities under either UV or visible light irradiation follow the order: FSZ-ZnSe3 > FSZ-ZnSe2 > FSZ-ZnSe4 > FSZ-ZnSe1 > FSZ-ZnSe0. This result illustrates that the overfull amount of ZnSe affects the synergistic effect between ZnO and ZnSe component in the FSZ-ZnSe photocatalyst. On the one hand, the shielding effect of overfull ZnSe decrease the effective catalytic sites of ZnO nanorod and the intensity of light irradiating on the surface of ZnO nanorod, reducing the generation of photo-generated electrons and holes [32]. On the other hand, overfull ZnSe inhibits the interfacial transition of electrons between ZnO and ZnSe, and then the separation rate of electron-hole pairs is reduced [18,30].

Interestingly, as revealed in Fig. 8c, the photocatalytic activity under visible light is much weaker than the activity under UV light for the same sample, such as FSZ-ZnSe3 sample (UV: 96.96%, Vis: 58.20%). In addition, the equation of pseudo-first order correlation $-\ln(C/C_0) = kt$ is used to fit above date, where k is the apparent reaction rate constant. Here, the apparent reaction rate constants under UV and
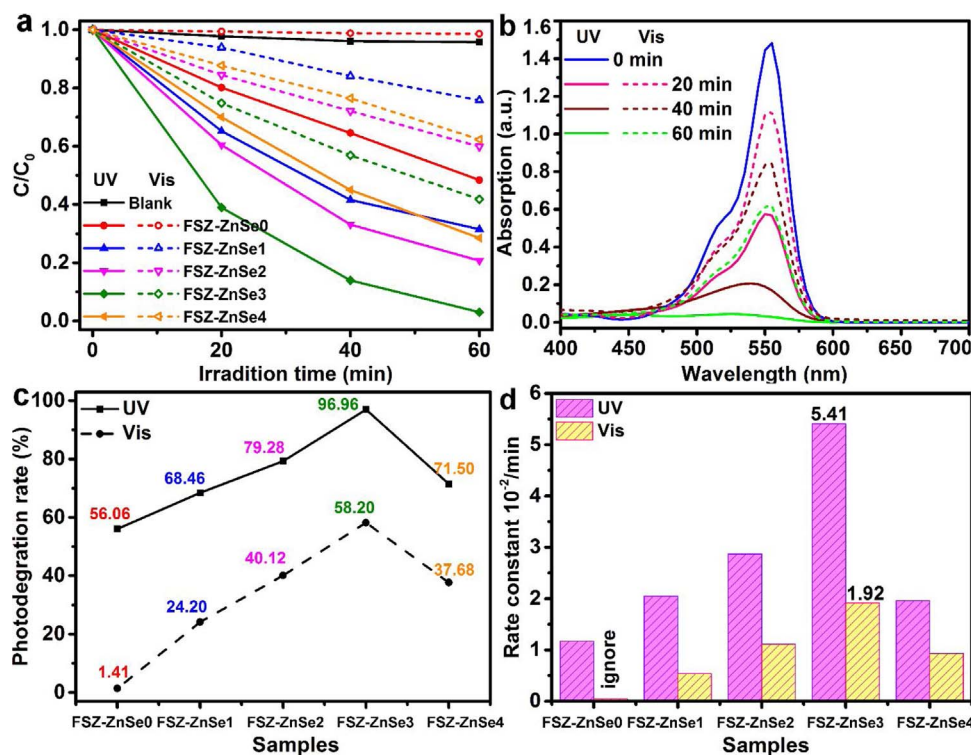

Fig. 8. Under UV or visible light irradiation: (a) photodegradation efficiency activity of various types of FSZ-ZnSe samples; (b) photocatalytic degradation curves of RhB over time with FSZ-ZnSe3 sample as photocatalyst; (c) final photodegradation rate of RhB and (d) rate constants for different FSZ-ZnSe samples.
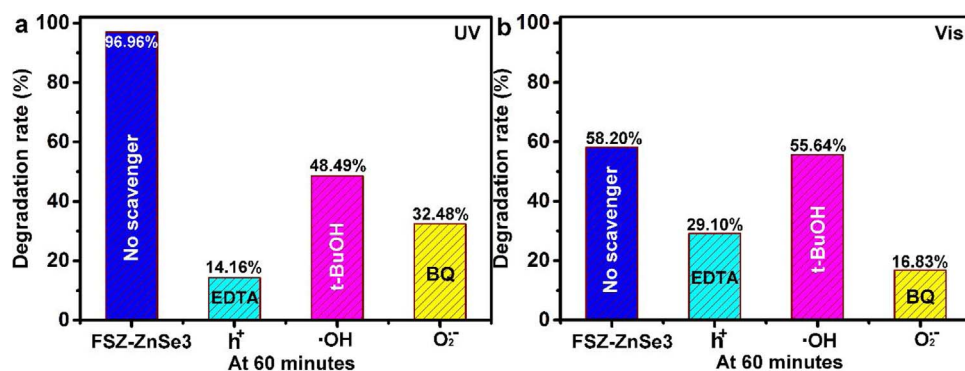
visible light irradiation are denoted as k and k', respectively. As shown in Fig. 8d, the k value is distinctly larger than k' value for the same sample. In particular, the k reaches a peak value of $5.41 \times 10^{-2}\,min^{-1}$ for FSZ-ZnSe3 sample, exceeding its k' ($1.92 \times 10^{-2}\,min^{-1}$) by a factor of 2.8.

3.6. Possible photocatalytic mechanism

The scavenging experiment was performed to study the role of active substance, including h^+, $\cdot OH$, and $O_2\cdot^-$, in the process of photocatalytic reaction. The scavenging experiment procedure was similar to the degradation experiment; various scavengers such as ethylenediaminetetraacetate (EDTA), tert-butyl alcohol (t-BuOH), and 1,4-benzoquinone (BQ) were introduced into the aqueous RhB before the addition of photocatalyst to scavenge the h^+, $\cdot OH$ and $O_2\cdot^-$, respectively [32,33]. Fig. 9a shows the results of scavenging experiment under UV light irradiation. After adding EDTA, t-BuOH and BQ scavengers, the degradation rate of RhB decreases from 96.96% (no scavenger) to 14.16% (EDTA), 48.49% (t-BuOH), and 32.48% (BQ), respectively. However, for visible light irradiation (Fig. 9b), the percentage degradation diminishes slightly from 58.20% (no scavenger) to 55.64% after the addition of t-BuOH, while the addition of EDTA and BQ scavengers greatly reduces the degradation rate to 29.10%, and 16.83%, respectively. Above dates indicate that h^+, $\cdot OH$, and $O_2\cdot^-$ are the fundamental reactive species for FSZ-ZnSe3 photocatalyst under UV light irradiation, while h^+ and $O_2\cdot^-$ play a crucial role in photocatalytic reaction for visible light irradiation, except for $\cdot OH$.

According to above investigation and physicochemical properties of ZnO and ZnSe, possible photocatalytic mechanisms of FSZ-ZnSe3 sample are illustrated in Scheme 1. For UV light irradiation, there are two possible routes for photo-excited carriers transfer, as shown in Scheme 1a and b. If the electron-hole pairs transfer following the heterojunction mechanism (Scheme 1a), $\cdot OH$ doesn't form by the reaction of the accumulated photo-generated holes in the valence band (VB) of ZnSe with adsorbed H_2O or $-OH$, due to the VB potential of ZnSe ($+2.16\,eV$) is lower than the required potential for $\cdot OH$ generation ($H_2O/\cdot OH = +2.4\,eV$, $-OH/\cdot OH = +2.7\,eV$) [26,34]. But, this is

contrary to above scavenging experimental result ($\cdot OH$ is the main active radical in photocatalytic reaction). Thus, the electron-hole transfer in ZnO/ZnSe heterostructure should follow basically Z-scheme mechanism [5,33]. As revealed in Scheme 1b, the photo-induced holes in ZnO tend to keep in the VB of ZnO (2.98 eV), whereas the electrons transfer to the VB of ZnSe (2.16 eV) from the conduction band (CB) of ZnO ($-0.39\,eV$), where they combine with the holes in the VB of ZnSe, and the photo-generated electrons of ZnSe remains mainly in its CB ($-0.64\,eV$). This leads to an efficient space separation between the photo-induced electrons and holes. Then, the holes in the VB of ZnO oxidize adsorbed H_2O or $-OH$ groups into highly reactive $\cdot OH$, while the electrons in the CB of ZnSe are trapped by O_2 near the surface of ZnSe to form reactive $\cdot O_2^-$ ($O_2/O_2\cdot^- = 0.28\,eV$). Finally, the RhB is degraded by these highly active radical species.

Scheme 1c presents the electron-transfer processes of FSZ-ZnSe3 photocatalyst under visible light illumination. Conduction band electronics and valence band holes are generated firstly in ZnSe crystals. The electronics transfer to the conduction band of ZnO by electron injection, and the holes remain in the ZnSe valence band, which decrease the probability of charges recombination. The electronics in ZnO react with O_2 on ZnO surface, forming a superoxide radical anion $\cdot O_2^-$. However, in virtue of the lower VB potential of ZnSe ($+2.16\,eV$), the accumulated photo-generated holes in the VB of ZnSe can't react with adsorbed H_2O or $-OH$ to form $\cdot OH$ radicals. It is possible that the holes themself directly oxidize the RhB molecules [28]. This consists with the result of scavenging experiment, namely, h^+ and $O_2\cdot^-$ are main active species under visible light illumination, except for $\cdot OH$. Therefore, it is not difficult to understand why the photocatalytic activity under visible light is much weaker than the activity under UV light for the same sample.

3.7. Hydroxyl radical determination

The $\cdot OH$ radical determination was used to confirm the proposed electron-transfer mechanisms of FSZ-ZnSe3 photocatalyst under UV and visible light irradiation. During UV light illumination, a gradual increase in fluorescence intensity at about 425 nm is observed with
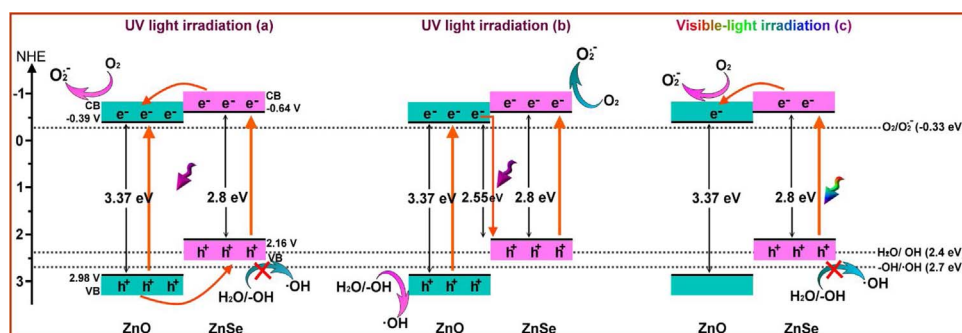
Scheme 1. Schematic diagram of the possible electron-transfer processes of FSZ-ZnSe3 photocatalyst under UV (a, b) and visible light (c) irradiation.
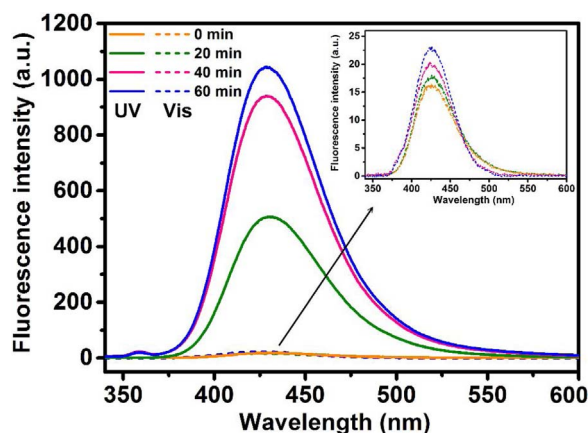
Fig. 10. Fluorescence spectral changes observed during UV and visible light illumination for the FSZ-ZnSe3 photocatalyst in a 5×10^{-4} M basic solution of TA. (Inset: the magnifying fluorescence spectral changes observed under visible light illumination).
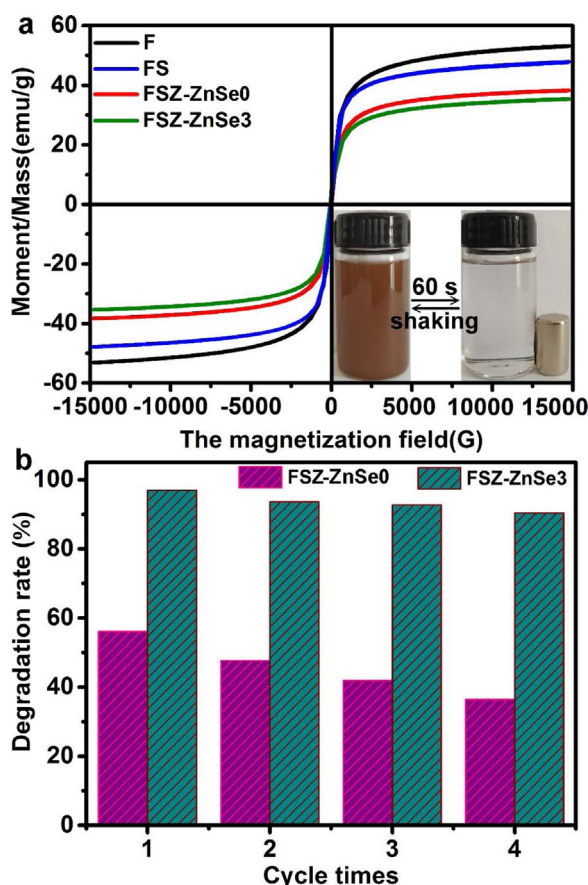

Fig. 11. (a) Room-temperature magnetization curves of F, FS, FSZ-ZnSe0 and FSZ-ZnSe3 products (Insert: the separation-redispersion process of FSZ-ZnSe3 in solution using a magnet). (b) The reusability of FSZ-ZnSe0 and FSZ-ZnSe3 samples under UV light illumination.

increasing irradiation time in Fig. 10, which indicates that the ·OH radicals are produced. And it is well known that h^+ mainly contributes to the generation of ·OH radicals [35]. Because there is hardly any ·OH that is formed by the heterojunction mechanism (Scheme 1a), this confirms that ZnO and ZnSe form a direct Z-scheme system (Scheme 1b) under UV light irradiation. However, as shown in the insert of Fig. 10, comparatively weak fluorescence signals are observed during visible light irradiation, indicating few ·OH radicals are produced by the reaction between h^+ in the VB of ZnSe and adsorbed H_2O or −OH. This

result is consistent with Scheme 1c, which presents the electron-transfer processes of FSZ-ZnSe3 photocatalyst under visible light illumination.

3.8. Magnetic properties and catalyst stability

Fig. 11a shows room-temperature magnetization curves of F, FS, FSZ-ZnSe0 and FSZ-ZnSe3 products. All magnetic hysteresis curves have no obvious remanence or coercivity, indicating the investigated samples possess superparamagnetic feature [21,22]. The saturation magnetization (Ms) value of F sample is measured as a control; it reaches 53.29 emu/g. The Ms value for FS, FSZ-ZnSe0 and FSZ-ZnSe3 samples decrease to be 47.88, 38.26 and 35.45 emu/g, respectively. The obviously reduced Ms value is mainly due to the non-magnetic SiO_2, ZnO and ZnSe content in FS, FSZ-ZnSe0 and FSZ-ZnSe3 samples. The superparamagnetic behavior and an adequate Ms value usually imply that magnetic material can be easily separated from solution by using an applied magnetic field and dispersed again after removing the external magnetic field [36]. In this regard, it can be noted from the inset in Fig. 11a that FSZ-ZnSe3 sample is quickly attracted to the side of the vial within 60 s when a magnet is used, leaving the solution transparent, and then the agminated FSZ-ZnSe3 sample disperses again by shaking after removing the magnet. So, FSZ-ZnSe3 photocatalyst would be suitable for magnetic separation and recovery.

The stability of FSZ-ZnSe0 and FSZ-ZnSe3 photocatalysts under UV light illumination was investigated. As shown in Fig. 11b, a relatively high stability is kept over FSZ-ZnSe3 photocatalyst (the photodegradation rate of RhB > 90% in 4 successive reactions) in the recycling photocatalytic experiments, whereas the photocatalytic activity of FSZ-ZnSe0 sample evidently weakens in the fourth run (from 56.06% to 36.41%). Above result illustrates the deposition of ZnSe particles not only improves the photocatalytic capacity FSZ-ZnSe0 sample, but also polishes up the cyclical stability.

4. Conclusions

In this study, a new three-dimensional multi-shell $Fe_3O_4/SiO_2/ZnO/ZnSe$ (FSZ-ZnSe) photocatalyst with a type II heterostructure was successfully fabricated. The loading density of ZnSe particles in the FSZ-ZnSe microspheres was controlled by changing reactant concentration. The cooperation of ZnSe and ZnO not only played a key role in enabling FSZ-ZnSe to act as a visible light driven photocatalyst, but also significantly enhanced the catalytic activity of FSZ-ZnSe under UV light due to the Z-scheme type transfer of photo-generated carriers. Moreover, among all the FSZ-ZnSe products (FSZ-ZnSe0, FSZ-ZnSe1, FSZ-ZnSe2, FSZ-ZnSe3 and FSZ-ZnSe4), the FSZ-ZnSe3 microspheres exhibited better activity either under UV or visible light, benefiting from the sensitization of a proper amount of ZnSe particles. Meanwhile, the FSZ-ZnSe3 photocatalyst was easily recovered by using a magnet, and had no obvious loss of catalytic activity in four cycles. This study demonstrates the guidance and potential for designing the composite materials with type II heterostructure for high-efficiency photocatalytic applications.

Appendix A. Supplementary data

Supplementary data associated with this article can be found, in the online version, at https://doi.org/10.1016/j.apcatb.2018.01.002.

References

[1] J. Wang, J.H. Yang, X.Y. Li, B. Feng, B. Wei, D.D. Wang, H.J. Zhai, H. Song, Effect of surfactant on the morphology of ZnO nanopowders and their application for photodegradation of rhodamine B, Powder Technol. 286 (2015) 269–275.

[2] M.L. Zhou, K. Xiao, X.X. Jiang, H.W. Huang, Z.S. Lin, J.Y. Yao, Y.C. Wu, Visible-light-responsive chalcogenide photocatalyst Ba$_2$ZnSe$_3$: crystal and electronic structure, thermal, optical, and photocatalytic activity, Inorg. Chem. 55 (2016) 12783–12790.

[3] Q.Z. Wang, Y.B. Shi, Y. Sun, H.D. She, J. Yu, Y.Y. Yang, Designed C$_3$N$_4$/CdS-CdWO$_4$ core-shell heterostructure with excellent photocatalytic activity, New J. Chem. 41 (2017) 1028–1036.

[4] K. Katsumata, R. Motoyoshi, N. Matsushita, K. Okada, Preparation of graphitic carbon nitride (g-C$_3$N$_4$)/WO$_3$ composites and enhanced visible-light-driven photodegradation of acetaldehyde gas, J. Hazard. Mater. 260 (2013) 475–482.

[5] J.M. Li, H.Y. Cheng, Y.H. Chiu, Y.J. Hsu, ZnO-Au-SnO$_2$ Z-scheme photoanodes for remarkable photoelectrochemical water splitting, Nanoscale 8 (2016) 15720–15729.

[6] D.D. Wang, J.H. Yang, X.Y. Li, J. Wang, J.H. Lang, J.S. Wang, H. Song, Preparation of morphology-controlled TiO$_2$ nanocrystals for the excellent photocatalytic activity under simulated solar irradiation, Mater. Res. Bull. 94 (2017) 38–44.

[7] L.J. Wang, H.J. Zhai, G. Jin, X.Y. Li, C.W. Dong, H. Zhang, B. Yang, H.M. Xie, H.Z. Sun, 3D porous ZnO-SnS p-n heterojunction for visible light driven photocatalysis, Phys. Chem. Chem. Phys. 19 (2017) 16576–16585.

[8] S. Cho, J.W. Jang, J. Kim, J.S. Lee, W. Choi, K.H. Lee, Three-dimensional type II ZnO/ZnSe heterostructures and their visible light photocatalytic activities, Langmuir 27 (2011) 10243–10250.

[9] D.F. Zhang, L.D. Sun, J. Zhang, Z.G. Yan, C.H. Yan, Hierarchical construction of ZnO architectures promoted by heterogeneous nucleation, Cryst. Growth Des. 8 (2008) 3609–3615.

[10] X.F. Zhou, Z.L. Hu, Y.Q. Fan, S. Chen, W.P. Ding, N.P. Xu, Microspheric organization of multilayered ZnO nanosheets with hierarchically porous structures, J. Phys. Chem. C 112 (2008) 11722–11728.

[11] P. Georgiev, N. Kaneva, A. Bojinova, K. Papazova, K. Mircheva, K. Balashev, Effect of gold nanoparticles on the photocatalytic efficiencyof ZnO films, Colloids Surf. A 460 (2014) 240–247.

[12] C. Eley, T. Li, F.L. Liao, S.M. Fairclough, J.M. Smith, G. Smith, S.C. Tsang, Nanojunction-mediated photocatalytic enhancement in heterostructured CdS/ZnO, CdSe/ZnO, and CdTe/ZnO nanocrystals, Angew. Chem. Int. Ed. 53 (2014) 7838–7842.

[13] Q. Luo, Z.M. Wu, J.L. He, Y.Y. Cao, W.A. Bhutto, W.P. Wang, X.L. Zheng, S.P. Li, S.Q. Lin, L.J. Kong, J.Y. Kang, Facile synthesis of composition-tuned ZnO/ZnxCd1-xSe nanowires for photovoltaic applications, Nanoscale Res. Lett. 10 (2015) 181.

[14] J.H. Yang, J. Wang, X.Y. Li, D.D. Wang, H. Song, Synthesis of urchin-like Fe$_3$O$_4$@SiO$_2$/ZnO/CdS core-shell microspheres for the repeated photocatalytic degradation of rhodamine B under visible light, Catal. Sci. Technol. 6 (2016) 4525–4534.

[15] Z.C. Wu, H. Wang, Y.J. Xue, B. Li, B.Y. Geng, ZnO nanorods/ZnSe heteronanostructure arrays with a tunable microstructure of ZnSe shell for visible light photocatalysis, J. Mater. Chem. A 2 (2014) 17502–17510.

[16] L. Chen, W.X. Zhang, C. Feng, Z.H. Yang, Y.M. Yang, Replacement/etching route to ZnSe nanotube arrays and their enhanced photocatalytic activities, Ind. Eng. Chem. Res. 51 (2012) 4208–4214.

[17] W. Chen, N. Zhang, M.Y. Zhang, X.T. Zhang, H. Gao, J. Wen, Controllable growth of ZnO-ZnSe heterostructures for visible-light photocatalysis, CrystEngComm 16 (2014) 1201–1206.

[18] B.T. Liu, L.L. Tian, Y.H. Wang, One-pot solvothermal synthesis of ZnSe.xN$_2$H$_4$/GS and ZnSe/N-GS and enhanced visible-light photocatalysis, ACS Appl. Mater. Interfaces 5 (2013) 8414–8422.

[19] M. Shekofteh-Gohari, A. Habibi-Yangjeh, Photosensitization of Fe$_3$O$_4$/ZnO by AgBr and Ag$_3$PO$_4$ to fabricate novel magnetically recoverable nanocomposites with significantly enhanced photocatalytic activity under visible-light irradiation, Ceram. Int. 42 (2016) 15224–15234.

[20] N. Li, J. Zhang, Y. Tian, J.H. Zhao, J. Zhang, W. Zuo, Precisely controlled fabrication of magnetic 3D γ-Fe$_2$O$_3$@ZnO core-shell photocatalyst with enhanced activity: ciprofloxacin degradation and mechanism insight, Chem. Eng. J. 308 (2017) 377–385.

[21] D.D. Wang, J.H. Yang, X.Y. Li, H.J. Zhai, J.H. Lang, H. Song, Preparation of magnetic Fe$_3$O$_4$@SiO$_2$@ZnO-Au spheres with well-designed microstructure and superior photocatalytic activity, J. Mater. Sci. 51 (2016) 9602–9612.

[22] D.D. Wang, J.H. Yang, X.Y. Li, J. Wang, H.J. Zhai, J.H. Lang, H. Song, Effect of thickness and microstructure of TiO$_2$ shell on photocatalytic performance of magnetic separable Fe$_3$O$_4$/SiO$_2$/mTiO$_2$ core-shell composites, Phys. Status Solidi A 1600665 (2017) 1–8.

[23] M. Kruk, M. Jaroniec, Gas adsorption characterization of ordered organic-inorganic nanocomposite materials, Chem. Mater. 13 (2001) 3169–3183.

[24] J.R. Huang, Y.J. Wu, C.P. Gu, M.H. Zhai, Y.F. Sun, J.H. Liu, Fabrication and gas-sensing properties of hierarchically porous ZnO architectures, Sens. Actuators B 155 (2011) 126–133.

[25] K. Wang, J.J. Chen, W.L. Zhou, Y. Zhang, Y.F. Yan, J. Pern, A. Mascarenhas, Direct growth of highly mismatched type II ZnO/ZnSe core/shell nanowire arrays on transparent conducting oxide substrates for solar cell applications, Adv. Mater. 20 (2008) 3248–3253.

[26] S.K. Yan, S.C. Rai, Z. Zheng, F. Alqarni, M. Bhatt, M.A. Retana, W.L. Zhou, Piezophototronic effect enhanced UV/visible photodetector based on ZnO/ZnSe heterostructure nanowire array and its self-powered performance, Adv. Electron. Mater. 2 (2016) 1600242.

[27] L.Y. Wang, G.H. Tian, Y.J. Chen, Y.T. Xiao, H.G. Fu, In situ formation of a ZnO/ZnSe nanonail array as a photoelectrode for enhanced photoelectrochemical water oxidation performance, Nanoscale 8 (2016) 9366–9375.

[28] X.T. Zhang, K.M. Ip, Z. Liu, Y.P. Leung, Q. Li, S.K. Hark, Structure and photoluminescence of ZnSe nanoribbons grown by metal organic chemical vapor deposition, Appl. Phys. Lett. 84 (2004) 2641–2643.

[29] Z.M. Wu, Y. Zhang, J.J. Zheng, X.G. Lin, X.H. Chen, B.W. Huang, H.Q. Wang, K. Huang, S.P. Li, J.Y. Kang, An all-inorganic type-II heterojunction array with nearly full solar spectral response based on ZnO/ZnSe core/shell nanowires, J. Mater. Chem. 21 (2011) 6020.

[30] H.W. Huang, Y. He, Z.S. Lin, L. Kang, Y.H. Zhang, Two novel Bi-based borate photocatalysts: crystal structure, electronic structure, photoelectrochemical properties, and photocatalytic activity under simulated solar light irradiation, J. Phys. Chem. C 117 (2013) 22986–22994.

[31] Y.B. Shi, Z.X. Yang, Y. Liu, J. Yu, F.P. Wang, J.H. Tong, B.T. Su, Q.Z. Wang, Fabricating g-C$_3$N$_4$/CuOx heterostructure with tunable valence transition for enhanced photocatalytic activity, RSC Adv. 6 (2016) 39774–39783.

[32] L.H. Xie, Z.Y. Ai, M. Zhang, R.Z. Sun, W.R. Zhao, Enhanced hydrogen evolution in the presence of plasmonic Au-photo-sensitized g-C$_3$N$_4$ with an extended absorption spectrum from 460 to 640 nm, PLoS One 11 (2016) e0161397.

[33] Y.X. Yang, Y.N. Guo, F.Y. Liu, X. Yuan, Y.H. Guo, S.Q. Zhang, W. Guo, M.X. Huo, Preparation and enhanced visible-light photocatalytic activity of silver deposited graphitic carbon nitride plasmonic photocatalyst, Appl. Catal. B 142–143 (2013) 828–837.

[34] X.F. Bian, K.Q. Hong, X. Ge, R. Song, L.Q. Liu, M.X. Xu, Functional hierarchical nanocomposites based on ZnO nanowire and magnetic nanoparticle as highly active recyclable photocatalysts, J. Phys. Chem. C 119 (2015) 1700–1705.

[35] W.K. Jo, T.S. Natarajan, Influence of TiO$_2$ morphology on the photocatalytic efficiency of direct Z-scheme g-C$_3$N$_4$/TiO$_2$ photocatalysts for isoniazid degradation, Chem. Eng. J. 281 (2015) 549–565.

[36] X.Q. Xu, C.H. Deng, M.X. Gao, W.J. Yu, P.Y. Yang, X.M. Zhang, Synthesis of magnetic microspheres with immobilized metal ions for enrichment and direct determination of phosphopeptides by matrix-assisted Laser desorption ionization mass spectrometry, Adv. Mater. 18 (2006) 3289–3293.